PCCP

Accepted Manuscript

ROYAL SOCIETY OF CHEMISTRY

www.rsc.org/pccp

Table of contents

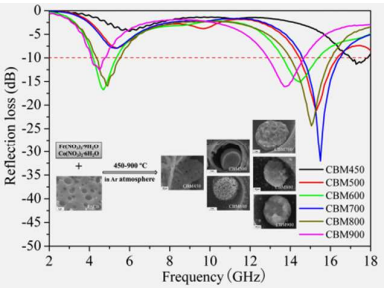

Microwave reflection loss -32 dB was obtained on lightweight composites of $CoFe_2O_4$ and/or Co_3Fe_7 particles within porous activated carbon balls.

PCCP

RSCPublishing

PAPER

$CoFe_2O_4$ and/or Co_3Fe_7 loaded Porous Activated Carbon Balls as a Lightweight Microwave Absorbent †

Cite this: DOI: 10.1039/xoxxoooooox

Received ooth January 2012,
Accepted ooth January 2012

DOI: 10.1039/xoxxoooooox

www.rsc.org/PCCP

Guomin Li,[ab] Liancheng Wang,[a] Wanxi Li,[ab] Ruimin Ding,[a] and Yao Xu[a]*

In order to prepare lightweight and efficient microwave absorbent, porous activated carbon balls (PACB) were used to load Fe^{3+} and Co^{2+} ions because PACB carrier has high specific surface area of 800 m^2/g and abundant pores including micropores and macropores. In the PACB composite, the loaded Fe^{3+} and Co^{2+} ions were transformed into magnetic $CoFe_2O_4$ and/or Co_3Fe_7 particles during the subsequent heat-treatment in Ar atmosphere. According to XRD and SEM results, the magnetic particles were embedded in the macropores of PACB and showed different crystalline phase and morphology after heat-treatment. The $CoFe_2O_4$ flakes with spinel structure were obtained around 450 ℃ and then transformed to loose quasi-spheres from 500 ℃ to 600 ℃ during which $CoFe_2O_4$ and Co_3Fe_7 coexisted because of the partial reduction of $CoFe_2O_4$. Co_3Fe_7 microspheres came into being after 700 ℃. The density of magnetic PACB composites was in the range of 2.2-2.3 g/cm^3. The as-synthesized PACB composites exhibited excellent microwave absorbability, mainly attributed to the magnetism of $CoFe_2O_4$ and Co_3Fe_7 as well as the existence of graphitized carbon. The minimum reflection loss value of $CoFe_2O_4/Co_3Fe_7$/PACB composite reached -32 dB at 15.6 GHz and the frequency of microwave absorption obeyed the quarter-wavelength matching model, showing a good match between dielectric loss and magnetic loss. The microwave reflection loss (RL) value could be modulated by adjusting the composition and thickness of PACB composites absorbent. PACB composites with $CoFe_2O_4/Co_3Fe_7$ are a promising candidate for lightweight microwave absorption materials.

1. Introduction

With the development of microwave detective technology, the microwave absorbing materials are facing lots of challenges and hence need to satisfy more and more new property designs including light-weight, strong microwave absorption, wide absorption bandwidth, and low cost. [1–3] Traditional single-component microwave absorbent cannot meet all the above property requirements simultaneously. Therefore light-weight composite materials containing both magnetic and dielectric absorbent become one of the main developing trends of microwave absorbing materials.

As an important material, carbon materials, including carbon black, carbon fibers, mesoporous carbon, activated carbon, carbon nanocoil, and carbon nanotubes, have been extensively explored as dielectric absorbents due to their low density and high electric conductivity. [4] However, poor permeability of carbon materials resulted in the mismatch of impedance and limited their extensive use. Therefore, it is quite essential to combine carbon materials with magnetic lossy fillers (Fe_3C, [5, 6] carbonyl-iron, [7] $CoFe_2O_4$, [8] Fe, [9–11] Co, [12] and Ni [13–15]) to form carbon-based composites, which can enhance the magnetic loss and improve impedance match. Wang et al. [16] synthesized the magnetic CNCs by coating magnetic Fe_3O_4 and Ni on the surface of CNCs using atomic layer deposition technique, and the as-prepared composite showed a much lower RL and wider absorption frequency range than pristine CNCS. There are also other ways to prepare the carbon-based materials, including electroless plating, [17] chemical vapor deposition (CVD) method, [18] and electrospinning technique. [19] However, complex process and high cost are the main disadvantages that the above technologies have to face. In contrast, the wet chemistry method is the most simple and versatile way in which carbon materials (MCNTs [20, 21]) were dispersed into single or mixed metal salt solution to produce magnetic carbon composites directly during heat-treatment.

Despite much attention focused on carbon-based absorbents, there were only a few reports on the microwave absorption involved with PACB. PACB used in our work possesses low density of about 1.77 g/cm^3 and abundant micropores and macropores with large specific surface area of 800 m^2/g and big pore volume of 1.66 cm^3/g, providing sufficient space to load magnetic absorbent. Another advantage of PACB is providing a reduction environment for oxides, with increasing temperature, $CoFe_2O_4$ could be steadily reduced into Co and Co_3Fe_7 by carbon atoms of PACB and the porous structure was still preserved. If controlling the heating temperature, we can obtain different composites as follows,

$CoFe_2O_4$/PACB, $CoFe_2O_4$/Co_3Fe_7/PACB, or Co/Co_3Fe_7/PACB. On the other hand, with partly graphitized structure, PACB showed conductivity to some extent and benefited the dielectric loss. Furthermore, the macropores within PACB provided a special confinement to prevent magnetic particles in pores from sintering together, which is similar to the role played by the channels of CNTs. [22, 23] Combining the magnetic loss, dielectric loss, and possibility of mass-production, PACB composite microwave absorbents may give us a new avenue in application.

2. Experimental

2.1 Materials preparation

The PACB used in our work was home-made in our institute. There are lots of micropores (diameter of pore is less than 2 nm) and macropores with diameter centered around 2.5 μm within PACB, and the pore size distribution is shown by supporting information Fig S1. In a typical synthesis, the PACB with an average diameter of 1 mm was first dispersed into the nitric acid solution (50 wt%) at 50 ℃ under stirring to increase the amount of oxygen-containing groups. After the suspension was centrifuged, the filtrated solid was washed with water until neutral and then dried at 105 ℃. The clear PACB was then dispersed in an aqueous solution of $Fe(NO_3)_3$•$9H_2O$ and $Co(NO_3)_2$•$6H_2O$ with the fixed Fe^{3+} and Co^{2+} ratio of 2:1, after draining excess water on the Busher funnel, the wet powder was dried at 60 ℃. Finally the dried powder was thermally treated from room temperature to 900 ℃ with a heating rate of 5 ℃/min in Ar atmosphere, and each temperature point was kept for 2 h. The final products were labeled as CBM400, CBM450, CBM500, CBM600, CBM700, CBM800, and CBM900 according to the thermal treating temperature.

2.2 Materials characterization

To reveal the crystallization structures of products, X-ray diffraction (XRD) measurement was performed on a D8 Advance Bruker AXS diffractometer, using Cu-Kα radiation (λ=1.5406 Å), employing a scan step of 0.01° in the 2θ range of 10 ° to 90 °. Thermogravimetry (TG) analysis was performed in a SETSYS EVOLUTION TGA 16/18 thermogravimetric analyzer. About 11 mg of sample was heated in Ar atmosphere with flow rate of 50 mL/min and heating rate of 5 ℃/min from 30 ℃ to 1000 ℃. A mass spectrometer (OMNI star GSD-200) was linked with the TG instrument to measure the gaseous compounds generated during pyrolysis and reduction process. The pore structure of the pristine PACB was measured with the mercury porosimeter (Micromeritics AUTOPORE 9500) and physisorption analyzer (Micromeritics ASAP 2020). The microscopic morphology of the samples was observed on scanning electron microscope (SEM, JSM-7001F). The element content was determined by the inductively coupled plasma emission spectroscopy (ICP, Thermo iCAP6300). Raman spectra were recorded on a Horiba LabRAM HR800 spectrometer with an Ar^+ laser. The magnetic properties were measured on a vibrating sample magnetometer (VSM Lakeshore Model 7400) at room temperature.

In order to investigate the microwave absorption property, the PACB composite was mixed with paraffin and then pressed into a cylindrical shaped compact (Φ_{outer} =7.0 mm and Φ_{inner} =3.0 mm). The electromagnetic parameters of the specimen with 25 wt% of the magnetic PACB composite were measured in 2-18 GHz range with a vector network analyzer (Agilent N5230) using transmission/reflection coaxial line method. Based on the above obtained complex permittivity and permeability in the measured frequency range, the RL coefficient (dB) of the electromagnetic wave (normal incidence) at the surface of a single-layer absorbent backed by a perfect conductor at a given frequency and layer thickness can be calculated according to transmission line theory. [24]

3. Results and discussion

3.1 Crystalline phase evolution in PACB composite

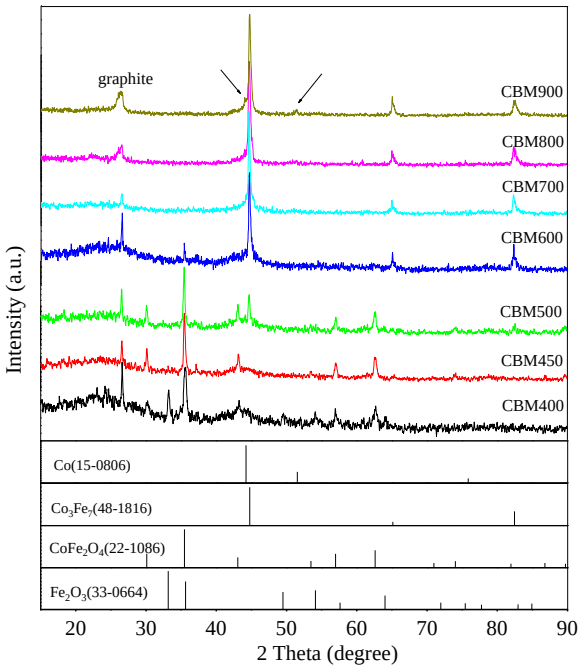

Fig. 1 XRD patterns of PACB composite treated at different temperature, where CBM400 to CBM900 means the products were treated from 400 ℃ to 900 ℃.

Figure 1 shows the XRD patterns of serial PACB composite treated at different temperatures. The detailed phase composition of the PACB composites obtained at different temperature is summarized in Table 1. The PACB composite treated less than 400 ℃ exhibits amorphous characteristics and therefore its XRD result is not collected in Figure 1. For the sample CBM400, the main diffraction peaks can be indexed as α-Fe_2O_3 (JCPDS No. 33-0664) and $CoFe_2O_4$ (JCPDS No. 22-1086). As the temperature increases to 450 ℃, the five characteristic peaks located at 2θ =30.1, 35.6, 43.8, 57.4, and 62.8 °become more obvious and can be attributed to the (220), (311), (440), (511), and (400) planes of $CoFe_2O_4$. This can also be confirmed by HRTEM image and the corresponding SAED pattern (shown by supporting information Fig S2). Compared with previous reports, [25, 26] the temperature 450 ℃ is somewhat lower for synthesis of $CoFe_2O_4$ because strong interaction between metal irons and pore wall of PACB through oxygen-containing groups benefits quick fusion of metal oxides to form $CoFe_2O_4$ after the decomposition of nitrates. In the temperature range of 500-600 ℃, the diffraction peaks of $CoFe_2O_4$ gradually disappear and the diffraction peaks of Co_3Fe_7 (JCPDS NO. 48-1816) appear, showing that $CoFe_2O_4$ was slowly reduced to alloy Co_3Fe_7 by carbon once the temperature exceeds 500 ℃. With further increasing temperature to 700-800 ℃, the only phase in the PACB composite becomes Co_3Fe_7.

From Figure 1, when temperature reaches 900 ℃, two additional weak peaks (see the arrow) appear and are indexed to the (111) and (200) planes of face-centered cubic phase of Co (JCPDS No. 15-0806). Based on the stoichiometric ratio, there should be Co in the XRD patterns of CBM700 and CBM800, the absence of Co may be due to the temperature is not high enough and the amount of Co is too low to detect. Furthermore, it's noted that there always exists a sharp diffraction peak at 2θ ≈26.5 °in all the XRD patterns, which can be indexed to (002) plane of graphite. [27]

Raman spectroscopy was used to calculate the degree of graphitization, that is, the relative intensity between the disordered carbon (turbostratic structure) and ordered carbon (graphite) within the PACB composites. Seen from supporting information Fig S3, it's evident that the variation of graphitization is negligible, confirming that the framework structure of PACB is not changed evidently.

Table 1. Magnetic properties, crystal phase, surface area and density [a] of PACB composites

	Ms (emu/g)	Mr (emu/g)	Hc (Oe)	Crystalline phase	Surface area (m^2/g)	ρ (g/cm^3)
PACB	—	—	—	—	801.2	1.77
CBM400	5.7	2.3	1423.5	α-Fe_2O_3/$CoFe_2O_4$	686.3	2.22
CBM450	17.3	2.6	157.1	$CoFe_2O_4$	605.5	2.31
CBM500	39.3	5.2	129.1	$CoFe_2O_4$/Co_3Fe_7	570.8	2.20
CBM600	57.9	7.5	234.9	$CoFe_2O_4$/Co_3Fe_7	421.2	2.23
CBM700	58.2	7.4	269.7	Co_3Fe_7	424.1	1.97
CBM800	57.5	7.3	327.8	Co_3Fe_7	382.4	2.24
CBM900	57.7	6.7	309.2	Co/Co_3Fe_7	340.9	2.23

[a] Saturation magnetization (Ms), remanent magnetization (Mr), and coercivity (Hc) were measured at room temperature. Density ρ was measured by pycnometer.

By analyzing the XRD results, serial reactions occurred during the pyrolysis process of PACB composites. However it is difficult to quantitatively distinguish these complex reactions only from XRD result. According to general inorganic chemistry theory, with increasing temperature, nitrate firstly decomposes into metal oxide, and then the two metal oxides sinter to produce ferrite, the metal finally formed via the carbon-thermal reduction. These reactions produced different gases at different reaction stages, which can be investigated by TG-MS technology. The detailed TG-MS result in Ar atmosphere is shown by Fig 2. The following gaseous species with different mass-to-charge ratio (m/z) were specially studied: NO (m/z=30), NO_2 (m/z=46), CO (m/z=28), CO_2 (m/z=44), and H_2O (m/z=18).

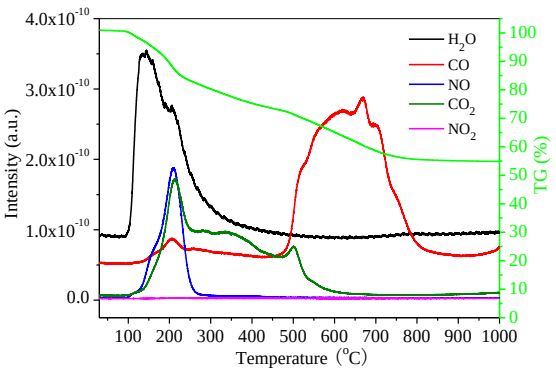

Fig. 2 TG-MS result of PACB composite.

From Figure 2, the TG curve shows a continuous and slow weight loss that can be divided into three stages: 30-300 ℃, 300-450 ℃ and 450-800 ℃. The first stage of weight loss of 30-300 ℃ is corresponding to evaporation of absorbed water and decomposition of crystal water in nitrates. There are two major peaks at 142 ℃ and 205 ℃ on the MS curve of H_2O, corresponding to the elimination of absorbed water and the step-wise removal of crystal water. The decomposition of $Fe(NO_3)_3$ occurred at about 175 ℃ before that of $Co(NO_3)_2$ at about 275 ℃, the reactions of nitrates decomposition are as followed equations (1) and (2). Lots of NO_2 produced in reaction (1) and (2) is easy to be reduced by carbon to release NO, CO and CO_2 like reaction (3) of which the reaction rate can be enhanced in the presence of H_2O and O_2. [28] Therefore, NO_2 was quickly consumed so that its intensity in MS curve is too low to detect, meanwhile, high peaks of NO, CO and CO_2 appeared in MS result. At this stage, the reactions between C and O_2 as well as C and H_2O cannot occur because 300 ℃ is not high enough.

$4Fe(NO_3)_3•9H_2O=2Fe_2O_3+12NO_2↑+9H_2O↑+3O_2↑$ (1)

$2Co(NO_3)_2•6H_2O=2CoO+4NO_2↑+6H_2O↑+2O_2↑$ (2)

$3NO_2+2C=3NO+CO+CO_2$ (3)

At the second stage of 300-450 ℃, Fe_2O_3 and CoO react together to form cobalt ferrite, as follows reaction (4). The oxygen-containing groups in PACB can be oxidized into CO_2 at this stage. [29, 30]

$Fe_2O_3+ CoO=CoFe_2O_4$ (4)

At the third stage of weight loss 450-800 ℃, there are the release of CO and CO_2. Combining with Figure 1 and Table 1, the major reaction should be the gradual carbon-thermal reduction of $CoFe_2O_4$ by carbon of PACB and the reduction products are Co and Co_3Fe_7, this reaction is shown by equation (5) and (6). According to the Ellingham Diagram, [31] CO is a more active reducing agent than C below 710 ℃, while C is more effective than CO at higher temperature. Therefore, the reaction (5) only occurred below 710 ℃, in which the peak of CO_2 exists. The CO peaks in MS curve between 600 ℃ and 700 ℃ result from the decomposition of phenolic hydroxyl group of PACB. [32]

$CoFe_2O_4+CO→Co_3Fe_7+CO_2↑$ (500 °C<T<710 ℃) (5)

$7CoFe_2O_4+28C=Co+2Co_3Fe_7+28CO↑$ (T>650 ℃) (6)

Above 800 ℃, no weight loss was observed and the gas release reached balance in the MS curves, implying that the reaction was completed.

3.2 Morphologies characterization

SEM was used to study the detailed microscopic structure and morphology of the PACB composite treated at different temperature, and the representative images are shown in Fig 3. For the morphology of original PACB, shown in Fig 3a, there are many smooth spherical macropores on the cross section of a single carbon ball. Fig 3b shows the cross section of CBM200, seen from which the pores were filled with dried nitrates and/or their decomposition products at 200 ℃. As can be seen from Fig 3c and 3d, plenty of flakes filled into the pores of PACB in the temperature range of 400-450 ℃, and the main composition of the flakes is $CoFe_2O_4$ (see Fig 1 and Table 1).

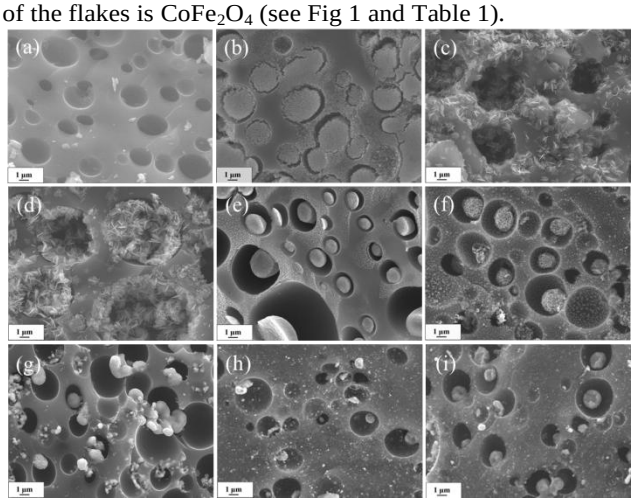

Fig. 3 SEM images of cross section of (a) PACB, (b) CBM200, (c) CBM400, (d) CBM450, (e) CBM500, (f) CBM600, (g) CBM700, (h) CBM800, and (i) CBM900.

The morphology of the products changed remarkably when the heat-treatment temperature increased to 500-700 ℃, seen from Fig 3e, 3f, and 3g, the flakes in CBM450 transform to the micron size particles and these particles show an interesting morphology evolution. The $CoFe_2O_4$ flakes of CBM450 sintered to form big particles just a little smaller than the pore size. From 500 ℃ to 600 ℃, these big particles located in the pores became smaller and looser, which may result from the continuous release of CO and CO_2 (see the TG-MS result in Fig 2). With further increasing temperature to 700 ℃, these small particles grew larger and became solid microspheres. After 800 ℃, the morphology had little change.

As can be seen from Fig 3b to Fig 3i, the cross section of the samples obtained at different temperature shows an obvious macropore distribution. As shown in Table 1, the surface area of the PACB composites displays a decreasing tendency with increasing of temperature. This mainly results from the blockage of the micropores of the PACB by the pyrolysis products of nitrates at first and then by the magnetic composition. However, the surface area of PACB composites is still larger than that of mesoporous $NiFe_2O_4$ absorber (121 m^2/g). [33] The density of PACB composite treated at different temperature maintains mainly in the range of 2.2-2.3 g/cm^3 (summarized in Table 1), exhibiting less noticeable variation. Compared with traditional magnetic microwave absorbent, the density of the above PACB composite is much lower, showing that PACB is an efficient framework for magnetic absorbent to reduce its density.

3.3 Magnetic properties

Magnetic parameters of the PACB composites are collected in Table 1. The magnetic hysteresis loops of all the samples at room temperature are showed in Fig S4 (supporting information), and all the magnetization curves exhibit typical ferromagnetic. From table 1, Ms and Mr increase initially with the calcination temperature and reach the maximum, then decrease a little. Taking the XRD result into account, the change of Ms and Mr should be attributed to the composition of the PACB composites, for Ms of $CoFe_2O_4$ is smaller than that of Co and Co_3Fe_7. [34–36] Additionally, elemental analysis from the ICP measurement gives the content of element Fe and Co are 19.24 wt% and 10.24 wt% in the PACB composite, with the rest mass as carbon. Therefore, the mass ratio of carbon is another reason cannot be neglected for the lower Ms. [37] As for Hc, its variation with the temperature is not in agreement with that of Ms and Mr. It is observed that the value of Hc for PACB composites is higher than the corresponding magnetic nanoparticles, which mainly results from the larger grain size and magnetocrystalline anisotropy. [38, 39]

3.4 Microwave absorption

The magnetization curves (see supporting information Fig S4) demonstrate that the PACB composites are ferromagnetic. To reveal the microwave absorption of the PACB composites, their RL was calculated using the measured complex permittivity ($\varepsilon_r=\varepsilon'-j\varepsilon''$) and complex permeability ($\mu_r=\mu'-j\mu''$) according to the following equations: [1, 16]

$$Z_{in} = \sqrt{\frac{\mu_r}{\varepsilon_r}} tanh\left[j\left(\frac{2\pi fd}{c}\right)\sqrt{\mu_r\varepsilon_r}\right] \quad (7)$$

$$\mathrm{R(dB)} = 20\lg\left|\frac{Z_{\mathrm{in}}-1}{Z_{\mathrm{in}}+1}\right| \quad (8)$$

where d is the thickness of the absorbent, f is the microwave frequency, c is the velocity of light, and Z_{in} is the input impedance of absorbent. From above analysis, the PACB composites can be divided into four classes according the phase composition, that is, $CoFe_2O_4$/PACB (CBM400, CBM450), $CoFe_2O_4$/Co_3Fe_7/PACB (CBM500, CBM600), Co_3Fe_7/PACB (CBM700, CBM800), and Co/Co_3Fe_7/PACB (CBM900). Therefore, we chose the representative three samples CBM450, CBM600, and CBM800 to investigate the microwave absorption. The thickness of coating is an important parameter affecting RL intensity and the frequency position of minimum absorption. [40] Consequently, we calculated the RL curve at different thickness of 1.5, 2.5, 3.5, 5, and 5.5 mm for each PACB composite. Figure 4 shows the RL curves of CBM450, CBM600, and CBM800 in the frequency range of 2-18 GHz. From Figure 4, there appear two RL dips at low and high frequencies simultaneously when the coating thickness exceeds 5 mm, while only one dip observed when the thickness is less than 5 mm. There is a quarter-wave thickness criteria between the absorbent thickness and peak frequency of an absorption dip: [41, 42]

$$\mathrm{t}_m = \frac{\lambda}{4\sqrt{|\varepsilon_r\mu_r|}} = \frac{c}{4f_m\sqrt{|\varepsilon_r\mu_r|}} \quad (9)$$

where t_m and f_m are the matching thickness and peak frequency of an absorption dip, λ and c are the wavelength of electromagnetic wave and light velocity. The comparison between the calculated value t_m^{cal} and experimental value t_m^{exp} of the PACB composites was shown in supporting information Fig S5, it's noted that they match well. Only when the microwave frequency $f=f_m$, $3f_m$, $5f_m$…, there would appear corresponding dips in the RL curve. Because of the limited testing frequency ranges (2-18 GHz), only one absorption dip observed in the RL curve when the coating thickness is less than 5 mm. Consequently, the microwave absorption dips coexisting at low and high frequency can be easily realized by changing the coating thickness. Compared with the complex

double-layer structural absorbers, [43, 44] this is also a facile and effective way to realize the dual-frequency microwave absorption.

In addition, as the coating thickness increases, the reflection peak moves forward the lower frequency region. For CBM450, there is only one weak peak at 17.3 GHz with the minimum RL of -12.6 dB when the thickness of the $CoFe_2O_4$/PACB composite is 5.5 mm. Whereas for CBM600, there are two RL dips when the coating thickness is 5 mm and 5.5 mm, which means the microwave absorption can be realized at both low and high frequency simultaneously. The minimum RL value of $CoFe_2O_4/Co_3Fe_7$/PACB composite is -17.4 dB occurred at 7.9 GHz with the thickness of 3.5 mm. The RL curve of CBM800 is similar to CBM600, and the main difference is RL value at low frequency is smaller than that at high frequency. A minimum RL value of -21 dB is observed at 14.5 GHz for Co_3Fe_7/PACB composite with a matching thickness of 5.5 mm. Besides, RL value of -10 dB means 90% microwave absorption and only the absorbent with RL value less than -10 dB can be considered in practical use. The corresponding bandwidth of above three samples during which the RL value is less than -10 dB is 1, 2.3, and 2.6 GHz. However, the difference of the microwave absorbability of these PACB composites is attributed to their different composition, and the existence of Co_3Fe_7 reduced by spinel $CoFe_2O_4$ enhances the magnetic loss, [45, 46] which is further confirmed by the magnetic loss tangent in Fig 7 described below.

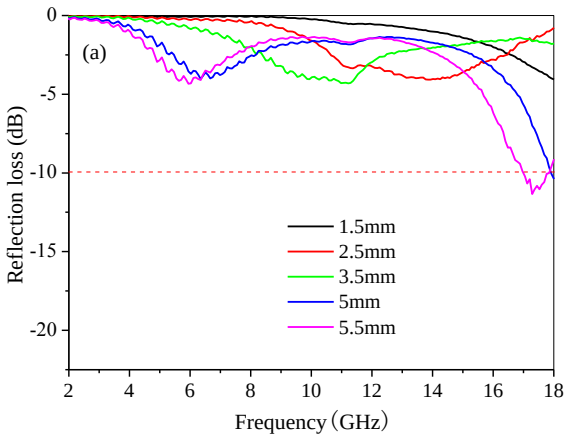

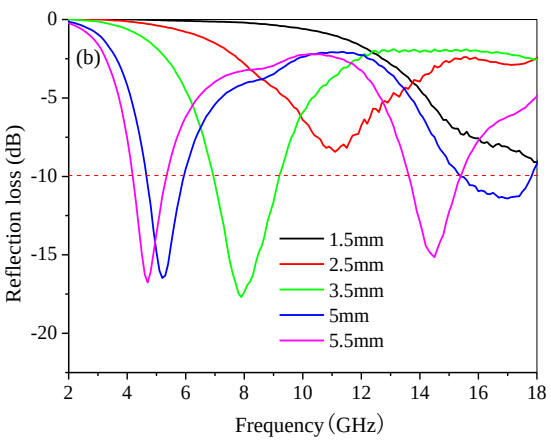

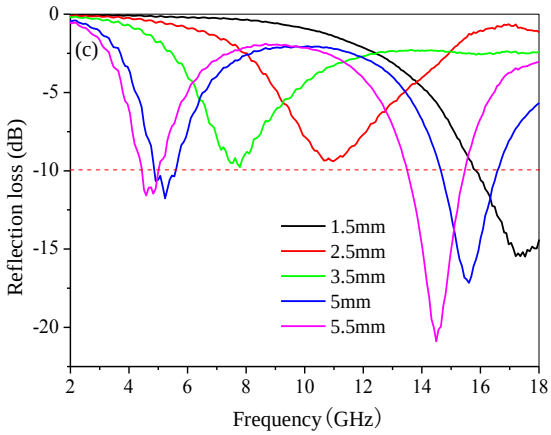

Fig. 4 Microwave RL curves of the PACB composites: (a) CBM450, (b) CBM600, and (c) CBM800 with different coating thickness.

Besides above mentioned thickness-dependent RL results of three representative PACB composites, the microwave absorption properties of all the samples were compared to study the influence of composition on the RL value by maintaining the same thickness of 5.5 mm, shown in Fig 5. It can be found that all these curves show two dips appeared at both C-band (4-8 GHz) and Ku-band (12-18 GHz) frequencies. The RL values less than -10 dB for both dips only existed in the curves of CBM600, CBM800, and CBM900. Moreover, the minimum RL of CBM450, CBM500, CBM600, CBM700, CBM800, and CBM900 are -11.1, -21.1, -16.7, -32.0, -24.4, and -16.1 dB at 17.4, 15.3, 4.7, 15.5, 15.0, and 13.7 GHz, respectively. That is to say the RL value can be modulated by changing the composition of the absorbent as well in our work. Consequently, the application diversification can be realized by adjusting the composition of absorbent according to the actual demand.

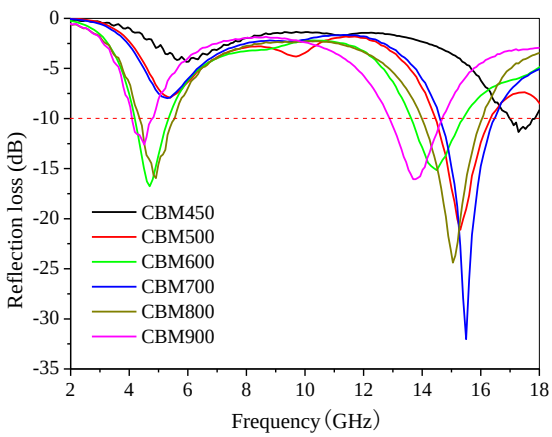

Fig. 5 Microwave RL curves of the PACB composites with a coating thickness of 5.5 mm.

3.5 Match of dielectric and magnetic loss

To disclose the intrinsic mechanism of microwave absorption of the PACB composites, the complex permittivity and complex permeability must be taken into consideration. Figure 6a shows the real part (ε') and imaginary part (ε'') of complex permittivity. It is known that ε' and ε'' represent the energy storage and dissipation capability, respectively. [47-49] For

CBM450 composite, it can be noted that the value of ε' and ε'' remain almost constant in the range of 2-10 GHz, and then decrease with increasing frequency. While the ε' value of CBM600 decreases from 10.7 to 7.5 in the range of 2-12 GHz and exhibits a slow increasing tendency at high frequency. For the CBM800 sample, the ε' value obviously declines initially with increasing frequency (from 11.5 to 7.6), followed by an increase to the initial value. In addition, the value of ε'' for both CBM600 and CBM800 exhibits the same variation trend as their respective ε' at the measured frequency (Figure 6a). According to the free electron theory, [20] $\varepsilon''=1/(2\pi\rho f\varepsilon_0)$, where ρ is the electric resistivity and ε_0 is the permittivity in vacuum, it can be speculated that lower ε'' of CBM450 means a higher electric resistivity than those of CBM600 and CBM800, resulted from the dispersed magnetic $CoFe_2O_4$ in the pores of PACB. This ultimately leads to poor microwave absorption of CBM450 compared with CBM600 and CBM800 (see Fig 4).

Figure 6b displays the real part (μ') and imaginary part (μ'') of complex permeability, respectively. For CBM450, a steady value is observed for μ' and μ'' in the lower frequency of 2-10 GHz, followed by a slow increase with increasing frequency, exhibiting rising trend. The real part μ' of complex permeability for CBM600 and CBM800 remains constant in the frequency range of 2-10 GHz and then shows some fluctuations at high frequency. As for μ'', an obvious resonance peak has been observed at around 15 and 16 GHz, correspondingly. It is generally agreed that, the magnetic loss of magnetic materials originates mainly from natural resonance, exchange resonance, magnetic hysteresis and eddy current loss in the microwave region. [50] The exist of eddy current loss can be decided by $\mu''\approx 2\pi\mu_0(\mu')^2\sigma d^2 f/3$, where μ_0 is the permeability in vacuum, d is the diameter of the nanoparticle and σ is electric conductivity. If the magnetic loss only originates from eddy current loss, equation $\mu''(\mu')^{-2}f^{-1}=2\pi\mu_0\sigma d^2/3$ should be constant. [51] The plot of $\mu''(\mu')^{-2}f^{-1}$ versus f was shown in supporting information Fig S6, $\mu''(\mu')^{-2}f^{-1}$ of CBM450 remains basically unchanged, revealing a typical eddy current loss. There are two obvious fluctuations for CBM600, confirming that magnetic loss of CBM600 is not caused by the eddy current loss. For CBM800, only one peak appears at high frequency, which may include a more complex loss mechamism. Besides, the obvious resonance peaks observed at high frequency in the μ'' curve of CBM600 and CBM800 (see Fig 6b) may be due to the exchange resonance according to Aharoni's theory, [52, 53] proven in ferromagnetic nanoparticles.

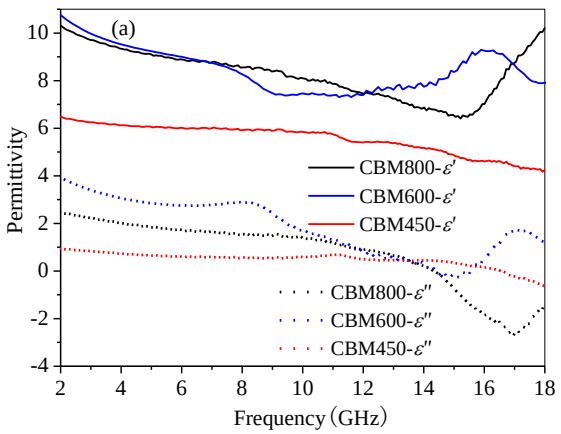

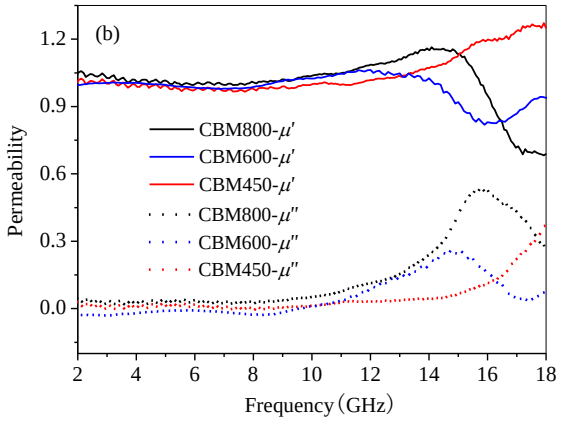

Fig. 6 Frequency dependence of (a) complex permittivity and (b) permeability of CBM450, CBM600 and CBM800.

In general, there are two possible contributions for microwave absorption, dielectric loss and magnetic loss. The dielectric and magnetic loss tangent can be expressed as $\tan\delta_e=\varepsilon''/\varepsilon'$ and $\tan\delta_m=\mu''/\mu'$. Figure 7 shows the frequency dependence of the loss tangents δ_e and δ_m for CBM450, CBM600, and CBM800. It's noted that δ_e and δ_m always coexist symmetrically and there is an intersection point at a specific frequency. The δ_m of CBM600 and CBM800 is larger than that of CBM450, showing that the Co_3Fe_7 can improve the magnetic loss. Therefore, in our case, the microwave absorption is ascribed to both dielectric loss and magnetic loss and their better match. However, this result is very different from previous report about RL on carbon nanotubes, [20] in which δ_m was monotonically larger than δ_e. Compared with other carbon materials, PACB possesses abundant micropores and macropores that can offer additional pathway for electromagnetic waves and thus cause multiple reflections, leading to enhanced microwave absorption. [54, 55]

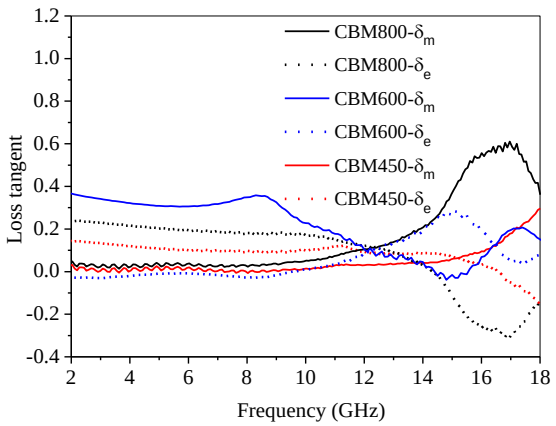

Fig. 7 Frequency dependence of the loss tangent of CBM450, CBM600 and CBM800.

4. Conclusions

The $CoFe_2O_4/Co_3Fe_7$/PACB composites were successfully prepared through wet chemistry method. The products possessed high specific surface area and exhibited excellent microwave absorbing performance, which resulted from better

match of magnetic and dielectric loss. The $CoFe_2O_4/Co_3Fe_7$/PACB composites are promising lightweight microwave absorbents that can be massively fabricated and are commercially feasible to be used as microwave absorbents since the simply technological operation.

Acknowledgements

The authors gratefully thank Prof. Kaixi Li for providing the porous activated carbon balls during the experiment. This work was supported by the National Science Foundation of ShanXi (No. 2012011005-1).

Notes and references

[a] Key Laboratory of Carbon Materials, Institute of Coal Chemistry, Chinese Academy of Sciences, Taiyuan 030001, China.
[b] University of Chinese Academy of Sciences, Beijing 100049, China.
† Electronic Supplementary Information (ESI) available. See DOI: 10.1039/b000000x/

1 J. M. Thomassin, X. D. Lou, C. Pagnoulle, A. Saib, L. Bednarz, I. Huynen, R. Jérôme and C. Detrembleur, *J. Phys. Chem. C*, 2007, **111**, 11186–11192.
2 X. G. Chen, Y. Ye and J. P. Cheng, *J. Inorg. Mater*., 2011, **26**, 449–457.
3 C. G. Hu, Z. Y. Mou, G. W. Lu, N. Chen, Z. L. Dong, M. J. Hu and L. T. Qu, Phys. Chem. Chem. Phys., 2013, **15**, 13038–13043.
4 F. Qin and C. Brosseau, *J. Appl. Phys*., 2012, **111**, 061301.
5 P. Xu, X. J. Han, X. R. Liu, B. Zhang, C. Wang and X. H. Wang, *Mater. Chem. Phys*., 2009, **114**, 556–560.
6 Q. M. Su, G. Zhong, J. Li, G. H. Du and B. S. Xu, *Appl. Phys. A*, 2012, **106**, 59–65.
7 M. W, Y. P. Duan, S. H. Liu, X. G. Li and Z. J. Ji, *J. Magn. Magn. Mater*., 2009, **321**, 3442–3446.
8 R. C. Che, C. Y. Zhi, C. Y. Liang and X. G. Zhou, *Appl. Phys. Lett*., 2006, **88**, 033105.
9 R. C. Che, C. Y. Liang, H. L. Shi, X. G. Zhou and X. N. Yang, *Nanotechnology*, 2007, **18**, 355705.
10 H. Y. Lin, H. Zhu, H. F. Guo and L. F. Yu, *Mater. Lett*., 2007, **61**, 3547–3550.
11 D. L. Zhao, X. Li and Z. M. Shen, *J. Alloys Compd*., 2009, **471**, 457–460.
12 Z. Zheng, B. Xu, L. Huang, L. He and X. M. Ni, *Solid State Sci*., 2008, **10**, 316–320.
13 I. M. De Rosa, A. Dinescu, F. Sarasini, M. S. Sarto and A. Tamburrano, *Comp. Sci. Tech*., 2010, **70**, 102–109.
14 J. J. Fang, S. F. Li, W. K. Zha, H. Y. Cong, J. F. Chen and Z. Z. Chen, *J. Inorg. Mater*., 2011, **26**, 467–471.
15 X. B. Feng, G. X. Liao, J. H. Du, L. M. Dong, K. J. Jin and X. G. Jian, *Polym. Eng. Sci*., 2008, **48**, 1007–1014.
16 G. Z. Wang, Z. Gao, S. W. Tang, C. Q. Chen, F. F. Duan, S. C. Zhao, S. W. Lin, Y. H. Feng, L. Zhou and Y. Qin, *ACS NANO*., 2012, **6**, 11009–11017.
17 K. Y. Park, J. H. Han, S. B. Lee and J. W. Yi, *Composites*: *Part A*, 2011, **42**, 573–578.
18 M. Terada, M. Itoh, J. R. Liu and K. I. Machida, *J. Magn. Magn. Mater*., 2009, **321**, 1209–1213.
19 Y. Yang, Z. Guo, H. Zhang, D. Q. Huang, J. L. Gu, Z. H. Huang, F. Y. Kang, T. A. Hatton and G. C. Rutledge, *J. Appl. Polym. Sci*., 2013, **127**, 4288–4295.
20 F. S. Wen, F. Zhang and Z. Y. Liu, *J. Phys. Chem. C*, 2011, **115**, 14025–14030.
21 F. S. Wen, F. Zhang, J. Y. Xiang, W. T. Hu, S. J. Yuan and Z. Y. Liu, *J. Magn. Magn. Mater*., 2013, **343**, 281–285.
22 X. L. Pan and X. H. Bao, *Acc. Chem. Res*., 2011, **44**, 553–562.
23 Z. J. Chen, Z. H. Guan, M. R. Li, Q. H. Yang and C. Li, *Angew. Chem*., 2011, **50**, 4913–4917.
24 R. F. Zhou, L. Qiao, H. T. Feng, J. T. Chen, D. Yan, Z. G. Wu and P. X. Yan, *J. Appl. Phys., 2008, **104**, 094101–094105.*
25 S. Briceño, W. Brämer-Escamilla, P. Silva, G. E. Delgado, E. Plaza, J. Palacios and E. Cañizales, *J. Magn. Magn. Mater*., 2012, **324**, 2926–2931.
26 C. Cannas, A. Musinu, D. Peddis and G. Piccaluga, *Chem. Mater*., 2006, **18**, 3835–3842.
27 Z. P. Zhou, C. L. Lai, L. F. Zhang, Y. Qian, H. Q. Hou, D. H. Reneker and H. Fong, *Polymer*, 2009, **50**, 2999–3006.
28 F. Jacquot, V. Logie, J. F. Brilhac and P. Gilot, *Carbon*, 2002, **40**, 335–343.
29 J. L. Figueiredo, M. F. R. Pereira, M. M. A. Freitas and J. J. M. Órfão, *Carbon*, 1999, **37**, 1379–1389.
30 M. S. Shafeeyan, W. M. A. W. Daud, A. Houshmand and A. Shamiri, *J. Anal. Appl. Pyrol*., 2010, **89**, 143–151.
31 M. Cavallini, *Appl. Phys. A*, 2013, **113**, 1049–1053.
32 U. Zielke, K. J. Hüttinger and W. P. Hoffman, *Carbon*, 1996, 34, 983–998.
33 X. Gu, W. M. Zhu, C. J. Jia, R. Zhao, W. Schmidt and Y. Q. Wang, *Chem. Commun*., 2011, **47**, 5337–5339.
34 M. Grigorova, H. J. Blythe, V. Blaskov, V. Rusanov, V. Petkov, V. Masheva, D. Nihtianova, Ll. M. Martinez, J. S. Muñoz and M. Mikhov, *J. Magn. Magn. Mater*., 1998, **183**, 163–172.
35 C. W. Kim, H. G. Cha, Y. H. Kim, A. P. Jadhav, E. S. Ji, D. I. Kang and Y. Soo Kang, *J. Phys. Chem. C*, 2009, **113**, 5081–5086.
36 Y. F. Li, Y. J. Hu, J. C. Huo, H. Jiang, C. Z. Li and G. J. Huang, *Ind. Eng. Chem. Res*., 2012, **51**, 11157–11162.
37 A. A. El-Gendy, E. M. M. Ibrahim, V. O. Khavrus, Y. Krupskaya, S. Hampel, A. Leonhardt, B. Büchner and R. Klingeler, *Carbon*, 2009, **47**, 2821–2828.
38 N. Poudyal, C. B. Rong and J. P. Liu, *J. Appl. Phys*., 2011, **109**, 07B526.
39 S. Mitra, S. Das, K. Mandal and S. Chaudhuri, *Nanotechnology*, 2007, **18**, 275608.
40 G. B. Sun, B. X. Dong, M. H. Cao, B. Q. Wei and C. W. Hu, *Chem. Mater*., 2011, **23**, 1587–1593.
41 B. C. Wang, J. Q. Wei, Y. Yang, T. Wang and F. S. Li, *J. Magn. Magn. Mater*., 2011, **323**, 1101–1103.
42 I. Kong, S. H. Ahmad, M. H. Abdullah, D. Hui, A. N. Yusoff and D. Puryanti, *J. Magn. Magn. Mater*., 2010, **322**, 3401–3409.
43 L. Y. Chen, Y. P. Duan, L. D. Liu, J. B. Guo and S. H. Liu, *Mater. Des*., 2011, **32**, 570–574.
44 M. Wang, Y. P. Duan, S. H. Liu, X. G. Li and Z. J. Ji, *J. Magn. Magn. Mater*., 2009, **321**, 3442–3446.
45 L. Xi, Z. Wang, Y. L. Zuo and X. N. Shi, *Nanotechnology*, 2011, **22**, 045707.

46 W. C. Li, X. J. Qiao, H. Zhao, S. M. Wang and Q. G. Ren, *J. Nanosci. Nanotechnol.*, 2013, **13**, 793–798.
47 J. E. Atwater and R. R. Wheeler, JR, *Appl. Phys. A*, 2004, **79**, 125–129.
48 C. Wang, X. J. Han, X. L. Zhang, S. R. Hu, T. Zhang, J. Y. Wang, Y. C. Du, X. H. Wang and P. Xu, *J. Phys. Chem. C*, 2010, **114**, 14826–14830.
49 S. Xie, X. N. Guo, G. Q. Jin and X. Y. Guo, *Phys. Chem. Chem. Phys*., 2013, **15**, 16104–16110.
50 J. Ma, J. G. Li, X. Ni, X. D. Zhang and J. J. Huang, *Appl. Phys. Lett.*, 2009, **95**, 102505.
51 F. S. Wen, H. B. Yi, L. Qiao, H. Zheng, D. Zhou and F. S. Li, *Appl. Phys. Lett.*, 2008, **92**, 042507.
52 G. Viau, F. Fievet-Vincent, F. Fievet, P. Toneguzzo, F. Ravel and O. Acher, *J. Appl. Phys*., 1997, **81**, 2749.
53 Ph. Toneguzzo, O. Acher, G. Viau, F. Fievet-Vincent and F. Fievet, *J. Appl. Phys*., 1997, **81**, 5546–5548.
54 G. Li, T. S. Xie, S. L. Yang, J. H. Jin and J. M. Jiang, *J. Phys. Chem. C*, 2012, **116**, 9196–9201.
55 G. X. Li, Y. X. Guo, X. Sun, T. Wang, J. H. Zhou and J. P. He, *J. Phys. Chem. Sol.*, 2012, **73**, 1268–1273.

